

Design of High-Speed Multilayer IPMSM Using Ferrite PM for EV Traction Considering Mechanical and Electrical Characteristics

Young-Hoon Jung^{ID}, Min-Ro Park^{ID}, Ki-O Kim, Jun-Woo Chin^{ID}, Jung-Pyo Hong^{ID}, Senior Member, IEEE, and Myung-Seop Lim^{ID}, Member, IEEE

Abstract—This article proposes a design method of the high-speed multilayer interior permanent magnet synchronous motor (HSML IPMSM) employing the ferrite permanent magnet (PM). Since the maximum speed of the traction motor in this article is 15 kr/min, the mechanical stability must be considered. Additionally, in the case of the HSML IPMSM, as the number of the PM layers increases, the thickness of the PMs must be reduced to be mechanically stable. On the other hand, because the ferrite PM has a relatively low coercive force compared with the Nd PM, an irreversible demagnetization of the ferrite PM of the HSML IPMSM is likely to occur. Therefore, the mechanical stability and irreversible demagnetization must be considered at all design steps. As the irreversible demagnetization and mechanical stability can be confirmed only by the finite-element analysis (FEA), the proposed method in this article is a design method that considers the irreversible demagnetization and mechanical characteristics at all design steps using the FEA. After the design of the traction motor is completed using this design method, the designed motor is manufactured. To verify the validity of the design method, experiments are conducted on the manufactured motor, and the test results are compared with FEA results.

Index Terms—Demagnetization ratio (DR), ferrite permanent magnet (PM), high-speed multilayer interior permanent magnet synchronous motor (HSML IPMSM), irreversible demagnetization, mechanical stability, rare-earth free motor, safety factor (SF), traction motor for electric vehicle (EV).

I. INTRODUCTION

RECENTLY, the increasing interest in electric vehicles (EVs) has increased the demand for electric motors that can replace the engines of the conventional vehicle. Such electric motors for driving a vehicle must satisfy the target power and

Manuscript received January 27, 2020; revised July 30, 2020; accepted September 29, 2020. Date of publication October 26, 2020; date of current version December 31, 2020. Paper 2019-EMC-1622.R1, presented at the 2019 IEEE Energy Conversion Congress and Exposition, Baltimore, MD USA, Sep. 29–Oct. 3, and approved for publication in the IEEE TRANSACTIONS ON INDUSTRY APPLICATIONS by the Electric Machines Committee of the IEEE Industry Applications Society. This work was supported by the National Research Foundation of Korea (NRF) grant funded by the Korea government(MSIT) (NRF-2020R1A4A4079701). (Corresponding author: Myung-Seop Lim.)

The authors are with the Department of Automotive Engineering, Hanyang University, Seoul 04763, South Korea (e-mail: yhjung207@hanyang.ac.kr; minro@kiro.re.kr; rldh529@hanyang.ac.kr; cjjw1254@hanyang.ac.kr; hongjp@hanyang.ac.kr; myungsop@hanyang.ac.kr).

Color versions of one or more of the figures in this article are available online at <https://ieeexplore.ieee.org>.

Digital Object Identifier 10.1109/TIA.2020.3033783

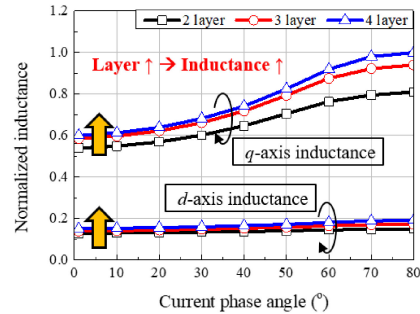


Fig. 1. Normalized inductance according to the number of the PM layers.

efficiency within a limited space in the vehicle; therefore, a high-power density and high-efficiency characteristics are required. An interior permanent magnet synchronous motor (IPMSM) using an Nd permanent magnet (PM) is one of the most attractive motors satisfying these characteristics [1]. The IPMSM using Nd PM is advantageous in reducing the size and input current of the motor to meet the same required power. This is because the IPMSM not only has a high magnetic torque owing to the Nd PM with the high residual induction but also has an additional reluctance torque that is caused by the difference in the *d*-axis and *q*-axis inductance. However, because of the limited production area of the rare-earth metals required to make the Nd PM, there is a problem that the supply of the Nd PM is unstable and the price fluctuation is large according to the international situation. Therefore, various studies have been made on the rare-earth free motors for replacing IPMSM using Nd PM.

Akhtar *et al.* [2]–[4] studied the induction motor to achieve high efficiency. Lee *et al.* [5]–[9] discussed the wound field synchronous motor having a high efficiency and torque. Liu *et al.* [10]–[13] discussed the optimal design and novel structures of the synchronous reluctance motor to achieve high torque and efficiency. In [14]–[17], various design methods to improve the torque density of the concentrated flux-type synchronous motor (CFSM) were presented. In addition to CFSM, multilayer IPMSM in which ferrite PM is arranged in multiple layers has been studied as the rare-earth free motor. As the number of PM layers of the multilayer IPMSM increases, the inductance difference between the *d*-axis and *q*-axis increases, as shown in Fig. 1, such that the reluctance torque can be increased. Therefore, the multilayer IPMSM using ferrite PM can be also an

alternative to IPMSM using Nd PM owing to its large reluctance torque.

Lim *et al.* [18]–[21] proposed the analysis and design method of the multilayer IPMSM using the equivalent magnetic circuit (EMC). The EMC is useful because it has the advantage of quickly identifying electrical characteristics, such as torque and loss, but it is difficult to determine whether the irreversible demagnetization is occurring. Especially, the local irreversible demagnetization can only be identified using the finite-element analysis (FEA). In the case of the ferrite PM, the irreversible demagnetization may easily occur than in the Nd PM because of its low coercive force. In addition, in the case of the multilayer IPMSM, since the PM thickness reduces as the number of PM layers increases, the multilayer IPMSM using the ferrite PM has a high possibility of the irreversible demagnetization. In general, the irreversible demagnetization of the PM is inspected after the design is completed, so if the irreversible demagnetization occurs, the design must be restarted from the beginning [22]. Therefore, when designing the multilayer IPMSM using ferrite PM, the irreversible demagnetization should be considered whenever necessary in the design process to prevent the excessive iteration of the design process. In [18]–[21], the mechanical characteristics were not considered. In [23], the mechanical stability of the high-speed multilayer IPMSM (HSML IPMSM) using the ferrite PM is presented but the detailed design process of the HSML IPMSM considering the mechanical stability is not proposed. In general, as in [23], the mechanical stability of the motor is examined at the end after reviewing its electrical characteristics. However, since the HSML IPMSM not only rotates at a high speed but also has a lot of stress concentrated areas in the rotor core, it is necessary to consider the mechanical characteristics at all design steps just as the irreversible demagnetization.

In this article, to examine the irreversible demagnetization and mechanical characteristics at all design stages of the HSML IPMSM, a design method employing FEA of the HSML IPMSM using the ferrite PM for the EV traction is proposed. As listed in Table I, the maximum rotational speed of the motor in this article is 15 kr/min, which is a high rotational speed; therefore, the mechanical stability should be considered as mentioned above. On the other hand, due to the high maximum rotational speed, the thickness of the PM of the HSML IPMSM decreases as the number of PM layers increases to satisfy the mechanical characteristics. As the thickness of the PM decreases, the possibility of generating the irreversible demagnetization of the PM increases; therefore, the irreversible demagnetization should also be considered at all design steps. In [24], the design method of HSML IPMSM is proposed but is not verified experimentally. Fig. 2 shows the design process of the HSML IPMSM using the ferrite PM presented in this article. First, to design the initial model, various design variables of the rotor are determined considering the mechanical stability and irreversible demagnetization. Second, the design for improving the electrical characteristics proceeds. The first part of the improved design is to prevent the irreversible demagnetization and improve the power factor to expand the satisfactory area of the target power. The second

TABLE I
BASIC INFORMATION

Content	Unit	Value	Note
Maximum speed	rpm	15000	-
Maximum torque	Nm	189	-
Maximum power	kW	120	-
Maximum current	A _{rms}	300	-
DC Voltage	V _{DC}	680	-
Pole number	-	8	-
Slot number	-	48	Changeable variable
Winding method	-	Distributed winding	Full pitch
Rotor core material	-	35PNT600Y	High strength steel
Stator core material	-	27PNX1350F	-
Residual induction	T	0.392	100°C
Demagnetization ratio	%	≤ 1	-
Safety factor	-	≥ 1.2	-

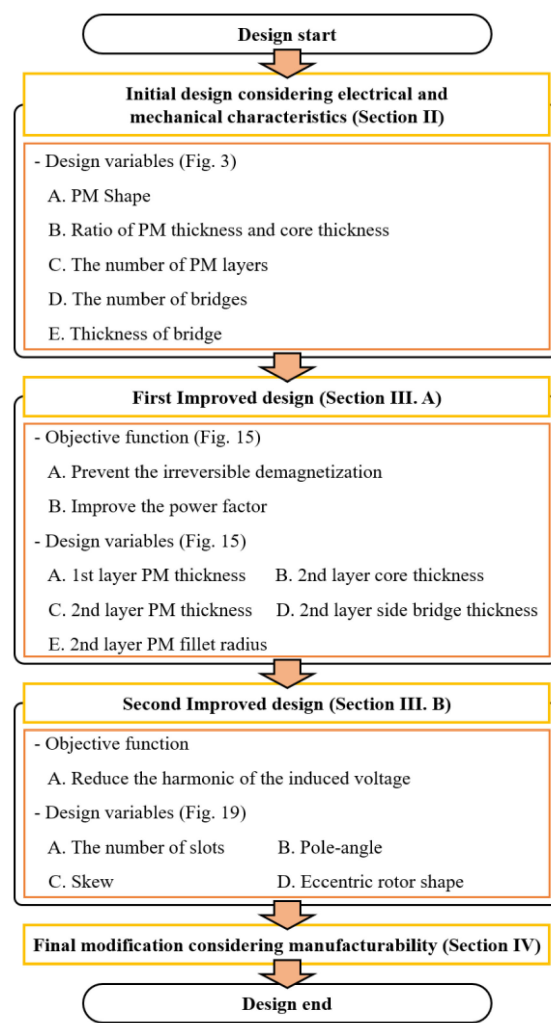


Fig. 2. Design process of HSML IPMSM using ferrite PM.

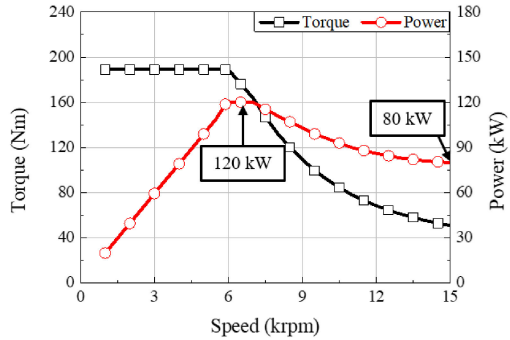


Fig. 3. Target torque and power according to the rotation speed.

part of the improved design is to reduce the harmonics of the induced voltage of the motor. Finally, the rotor shape is modified considering the fabrication, and the design of the HSML IPMSM using the ferrite PM is completed. Finally, the designed motor is fabricated and tested. To verify the proposed design method, the experimental results of the torque according to the rotation speed are compared with the results of the simulation.

II. INITIAL DESIGN OF HSML IPMSM CONSIDERING ELECTRICAL AND MECHANICAL CHARACTERISTICS

A. Design Specification and Analysis Condition

The basic information of the motor in this article is summarized in Table I. The maximum rotation speed is 15 kr/min. The maximum torque and power are 189 N·m and 120 kW, respectively. Fig. 3 shows the target torque and power according to the rotation speed. To input the sinusoidal current into the motor at the maximum speed, the number of poles is selected as eight so that the number of the switch ON/OFF of the inverter is 20 at the maximum speed. The number of slots is determined as 48 considering the electrical characteristics and vibration but this design variable can be changed. The winding method and coil pitch are distributed winding and full-pitch winding, respectively. Because of the high rotation speed of the motor, 35PNT600Y, which is a high strength steel, is used for the rotor core. 35PNT600Y has a thickness of 0.35 mm and a yield stress of 620 MPa. The core material of the stator is 27PNX1350F, which has a thickness of 0.27 mm. The core loss of 27PNX1350F is 13.5 W/kg when the flux density is 1.0 T at 400 Hz. The residual induction of the ferrite PM used in this article is 0.392 T at 100 °C. Since the coercive force of the ferrite PM decreases with decreasing the temperature, the lower the temperature, the easier it is for the irreversible demagnetization of the ferrite PM to occur. For this reason, the irreversible demagnetization is examined at -40 °C [25]. To determine the occurrence of the irreversible demagnetization, a demagnetization ratio (DR) is introduced in this article. The DR is expressed as

$$DR (\%) = \frac{\lambda_{ph,after} - \lambda_{ph,before}}{\lambda_{ph,before}} \times 100 \quad (1)$$

where $\lambda_{ph,after}$ is the peak value of the no-load phase linkage flux after the demagnetization analysis; $\lambda_{ph,before}$ is the peak value

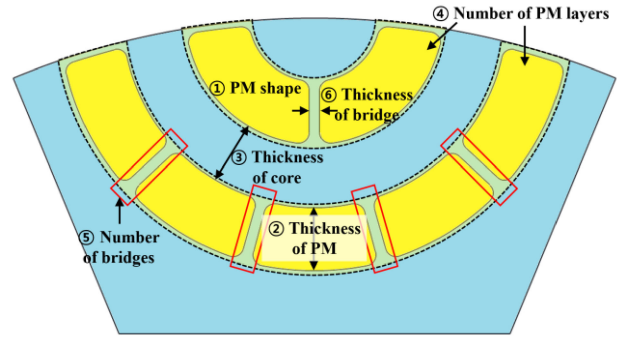


Fig. 4. Design variables of the rotor of HSML IPMSM.

of the no-load phase linkage flux before the demagnetization analysis. The demagnetization analysis is the load analysis considering the demagnetization curve of PM [26]. In this article, when the DR is less than 1%, it is determined that the irreversible demagnetization has not occurred. The mechanical stability is assessed as the safety factor (SF), which is used to account for uncertainties in the determination of the strength of a part as well as uncertainties in the evaluation of the stresses in a part [27]. The SF is expressed as

$$SF = \frac{\sigma_y}{\sigma_{max}} \quad (2)$$

where σ_y is the yield stress, which is the value at which the material begins to acquire inelastic or permanent deformation; σ_{max} is the maximum stress applying to the rotor due to the rotation. Since the yield stress is the value at which the material begins to acquire inelastic or permanent deformation, it means that the material becomes permanently deformed when SF is less than one. Therefore, to prevent the permanent deformation of the material, SF is determined one or more. In this article, when the SF is higher than 1.2, the rotor is considered to be mechanically stable [28].

The design variables of the rotor of the HSML IPMSM using the ferrite PM affect the electrical and mechanical characteristics of the HSML IPMSM. Therefore, in this section, the PM shape, PM thickness, core thickness, number of PM layers, number of bridges, and bridge thickness of the initial model are determined considering the electrical and mechanical characteristics. In other words, in this article, an objective of the initial design is appropriately determining the dimension of the design variables for satisfying the target torque, maximizing the SF, and minimizing the DR. The design variables considered in the initial design are shown in Fig. 4. During the initial design of the motor, the characteristics examined in this section are the no-load back electromotive force (BEMF), torque, DR, and SF. The no-load BEMF is obtained under the no-load condition at 1000 r/min. The torque is obtained under 300 A_{rms} and 45° because HSML IPMSM has a large reluctance torque. To calculate the DR, the demagnetization analysis is conducted under 1.2× the maximum current. Additionally, to assume the worst condition, the current phase angle is determined to be 90° such that the armature reaction is applied to the negative d-axis. The SF is obtained under the condition of 1.2× the maximum speed using the mechanical

TABLE II
ANALYSIS CONDITION OF INITIAL DESIGN

Content	Current (A _{rms})	Current phase angle (°)	Rotation speed (rpm)
No-load BEMF	-	-	1000
Torque	300	45	-
Demagnetization ratio	300 × 1.2	90	-
Safety factor	-	-	15000 × 1.2

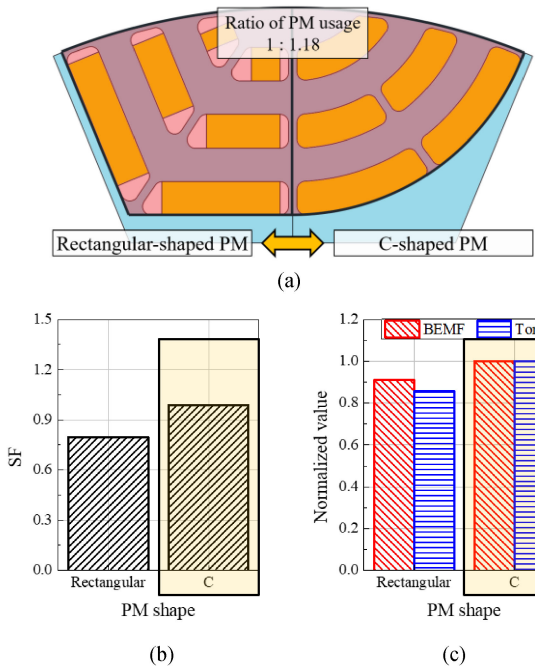


Fig. 5. Rotor shape, and mechanical and electrical characteristics according to the PM shape. (a) Rotor shape. (b) Mechanical characteristics. (c) Electrical characteristics.

field FEA [29]. The analysis conditions for obtaining the DR and SF are the internal standard of our laboratory determined empirically. The analysis conditions for examining each of the characteristics are summarized in Table II. The electromagnetic field FEA is conducted by the nonlinear analysis considering the magnetic saturation of the core. In addition, the transient analysis with respect to the time is used for the nonlinear FEA. The input current used in the FEA is the ideal sinusoidal current without considering the pulsedwidth modulation. The mechanical field FEA is analyzed using the structural analysis of the Ansys Workbench.

B. PM Shape

The PM shape affects the mechanical characteristics. Generally, the PM shape used in the IPMSM is a rectangular, but in this article, a C-shaped PM is used. Fig. 5(a) shows the rotor of the multilayer IPMSM using the rectangular-shaped and C-shaped PM. The maximum stress applied to the motor decreases as the pole piece area [red area in Fig. 5(a)] decreases [30]. As shown in Fig. 5(a), it can be seen that the PM usage of the C-shaped

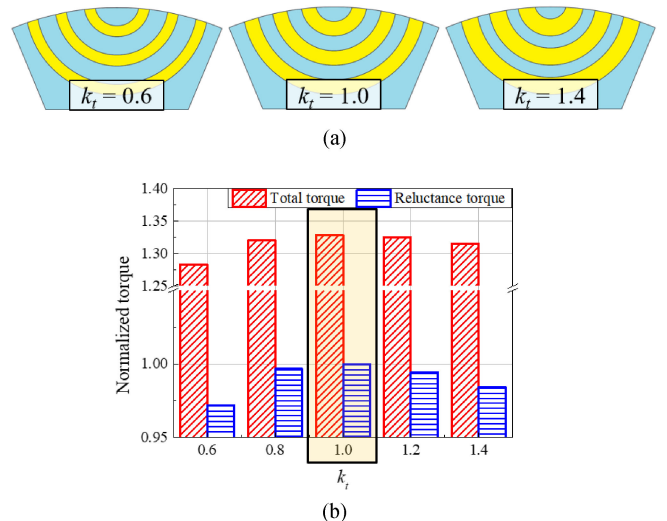


Fig. 6. Rotor shape and torque according to the ratio of PM thickness and core thickness. (a) Rotor shape. (b) Torque.

PM is about 18% larger than that of the rectangular-shaped PM, although the pole piece area of the C-shaped PM is smaller than that of the rectangular-shaped PM. Fig. 5(b) shows the SF of both models. As shown in Fig. 5(b), when the C-shaped PM is used, the maximum stress is reduced and the SF is increased because the pole piece area of the C-shaped PM is smaller than that of the rectangular-shaped PM. Fig. 5(c) shows the BEMF and torque of the HSML IPMSM using the two PM shapes. As shown in Fig. 5(c), the electrical characteristics, such as the BEMF and torque of the C-shaped PM, are better than those of the rectangular-shaped PM because the PM usage of the C-shaped PM is increased above that of the rectangular-shaped PM. Therefore, the PM shape used in this article is determined to be the C-shaped PM because the C-shaped PM is not only mechanically stable but also better the electrical characteristics than the rectangular-shaped PM.

C. Ratio of PM Thickness and Core Thickness

The ratio of the PM thickness and core thickness is determined considering the torque characteristics because the PM thickness affects the reluctance torque. The ratio of the PM thickness and core thickness is expressed as

$$k_t = \frac{t_{PM}}{t_c} \quad (3)$$

where k_t is the ratio of the PM thickness and core thickness; t_{PM} is the PM thickness; t_c is the core thickness. The total sum of the PM thickness and core thickness is the same, although k_t changes. In this section, since the number and thickness of bridges to be determined in the latter section affect the electrical characteristics, the bridges are ignored to exclude an effect of bridges on the electrical characteristics. Also, because the bridges are ignored, the mechanical characteristics are not considered. Fig. 6(a) and (b) show the rotor shape and torque characteristics according to k_t , respectively. In Fig. 6(b), the normalized torque is obtained dividing the torque according to

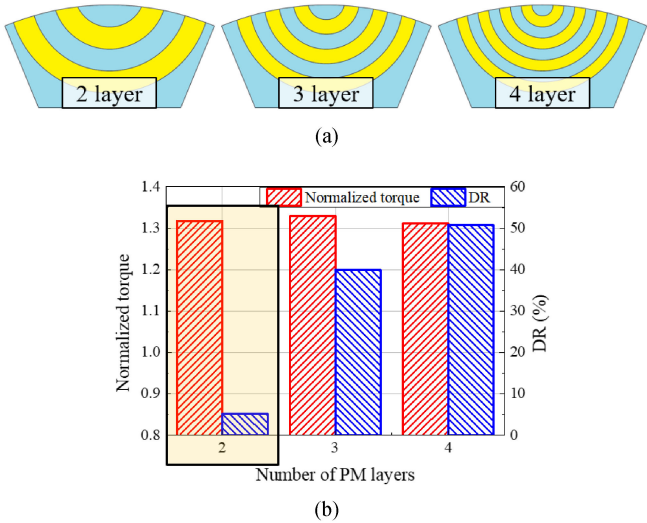


Fig. 7. Rotor shape and electrical characteristics according to the number of PM layers. (a) Rotor shape. (b) Electrical characteristics.

k_t into the target torque. As shown in Fig. 6(b), when $k_t = 1.0$, the reluctance torque and total torque are in their maximum values. Therefore, the ratio of the PM thickness and core thickness is selected to 1.0.

D. Number of PM Layers

The number of PM layers is determined by considering the torque characteristics and irreversible demagnetization. Fig. 7(a) shows the rotor shape according to the number of PM layers. The PM thickness decreases as the number of PM layers increases but the total PM thickness is the same for all models. As shown in Section II-C, the bridges are ignored to exclude an effect of bridges on the electrical characteristics. Since the bridges of all the models are neglected, the mechanical characteristics are not considered. The normalized torque and DR are shown in Fig. 7(b). In Fig. 7(b), the normalized torque is obtained dividing the torque according to the number of PM layers into the target torque. As shown in Fig. 7(b), the total torque of two layers is not significantly different from that of the other layers. However, since the PM thickness decreases with the increase in the number of PM layers, the DR of two layers is much smaller than that of the other layers. Therefore, the number of PM layers is selected as two, which is advantageous to prevent the irreversible demagnetization.

E. Number of Bridges

The number of bridges affects the mechanical and electrical characteristics. Fig. 8(a) shows the rotor shape according to the number of bridges. At this step, the thickness of the bridges is 1.0 mm. The SFs according to the number of bridges are shown in Fig. 8(b). As shown in Fig. 8(b), the SF increases with the increase in the number of bridges. Fig. 8(c) shows the DR and normalized torque according to the number of bridges, and the normalized torque is obtained dividing the torque according

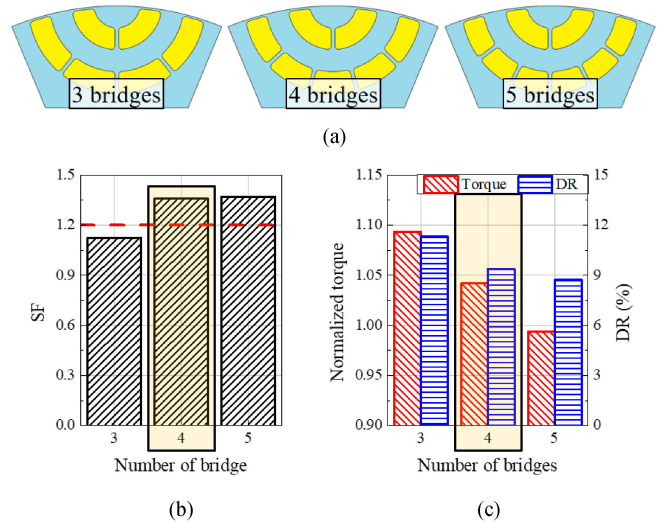


Fig. 8. Rotor shape, and mechanical and electrical characteristics according to the number of bridges. (a) Rotor shape. (b) Mechanical characteristics. (c) Electrical characteristics.

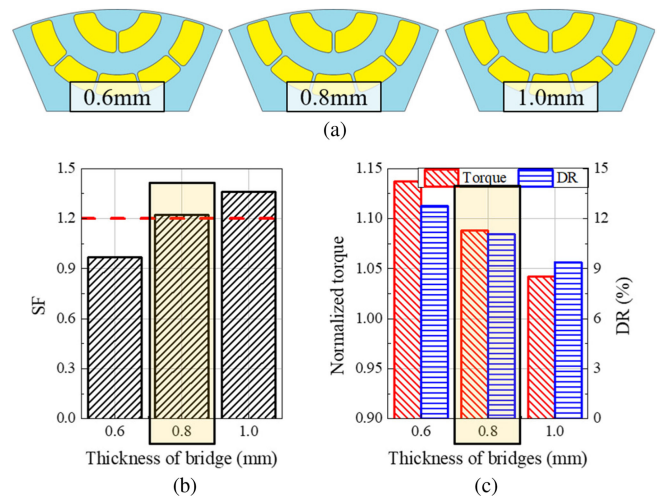


Fig. 9. Rotor shape, and mechanical and electrical characteristics according to the thickness of bridges. (a) Rotor shape. (b) Mechanical characteristics. (c) Electrical characteristics.

to the number of bridges into the target torque. As shown in Fig. 8(c), the DR and torque decrease, as the number of bridges increases. When the number of bridges is four or five, the SF is satisfied, and the DR has a similar value. However, the torque of the model with four bridges is larger than that of the model with five bridges. Therefore, the number of the bridges is selected as four.

F. Thickness of Bridges

Like the number of bridges, the thickness of bridges also affects the mechanical and electrical characteristics. Fig. 9(a) shows the rotor shape according to the thickness of the bridges.

Fig. 9(b) and (c) shows the SF and electrical characteristics, respectively. In Fig. 9(c), the normalized torque is obtained dividing the torque according to the thickness of bridges into the target torque. As the thickness of the bridges decreases, the SF decreases, and the torque and DR increase. The relation between the torque and DR is the tradeoff relation. In this article, among the models satisfying the mechanical characteristics, a model having a larger torque is selected. Therefore, the thickness of bridges is determined to be 0.8 mm.

G. Performance Curve of Initial Model

The initial model is designed through Section II-A–E. The rotor shape of the initial model is the rotor shape in the middle of Fig. 9(a). The SF and DR of the initial model are 1.22 and 11.1%, respectively. Since the DR is 11.1%, the irreversible demagnetization occurs. Thus, the improved design to reduce the DR is performed in the following section. The performance curve, including the torque and power according to the rotation speed, is calculated using the d - and q -axis equivalent circuit [9], [14]. To accurately calculate the performance of the motor, the end winding leakage inductance is considered. The end winding leakage inductance is expressed as [31]

$$L_{\text{end}} = 2.4 \times 4\mu_0 \frac{N_s^2}{P} k_w^2 \frac{l_{e1}}{2} \quad (4)$$

where L_{end} is the end winding leakage inductance; μ_0 is the permeability of the vacuum; N_s is the number of series turns; P is the number of poles; k_w is the winding factor of the fundamental component; l_{e1} is the end winding height. The end winding leakage inductance calculated using (4) is reflected in the d - and q -axis inductance as

$$L_{d,\text{end}} = L_d + \frac{3}{2}L_{\text{end}}, \quad L_{q,\text{end}} = L_q + \frac{3}{2}L_{\text{end}} \quad (5)$$

where $L_{d,\text{end}}$ and $L_{q,\text{end}}$ are the d - and q -axis inductance considering the end winding leakage inductance, respectively; L_d and L_q are the d - and q -axis inductance. $L_{d,\text{end}}$ and $L_{q,\text{end}}$ calculated using (5) are reflected in the d - and q -axis equivalent circuit and used to calculate the performance of the motor. The performance of the motor is calculated using the d - and q -axis equivalent circuits of the synchronous motor, which are shown in Fig. 10. Since the d - and q -axis equivalent circuits are generally considered only the fundamental component of the electrical parameters, the motor performance can be quickly reviewed. The performance of the motor, including the torque, induced voltage, and input current of the d - and q -axis equivalent circuits is calculated using the following equations:

$$T = pp \{\psi_f i_{oq} + (L_{d,\text{end}} - L_{q,\text{end}}) i_{od} i_{oq}\} \quad (6)$$

$$V_a = \sqrt{v_d^2 + v_q^2} = \sqrt{(R_a i_d + v_{od})^2 + (R_a i_q + v_{oq})^2} \quad (7)$$

$$I_a = \frac{1}{\sqrt{3}} \sqrt{i_d^2 + i_q^2} \quad (8)$$

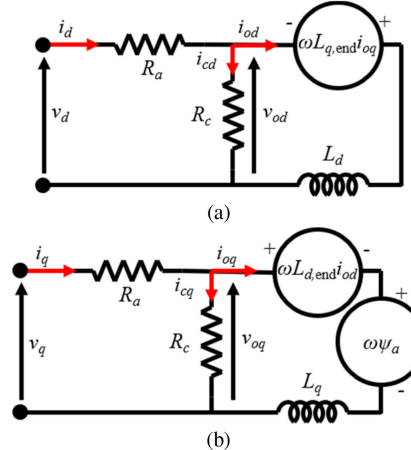


Fig. 10. Equivalent circuit of the synchronous motor. (a) d -axis. (b) q -axis.

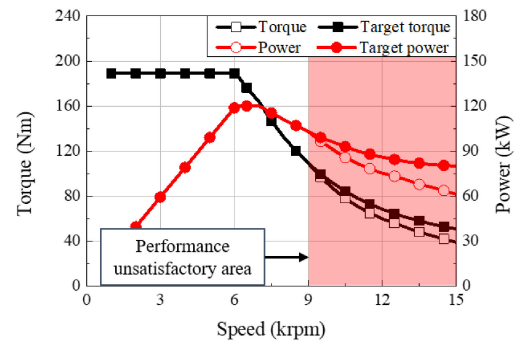


Fig. 11. Torque and power according to the rotation speed of the initial model.

where

$$\begin{bmatrix} v_{od} \\ v_{oq} \end{bmatrix} = \begin{bmatrix} 0 & -\omega L_{q,\text{end}} \\ \omega L_{d,\text{end}} & 0 \end{bmatrix} \begin{bmatrix} i_{od} \\ i_{oq} \end{bmatrix} + \begin{bmatrix} 0 \\ \sqrt{3}\omega\psi_f \end{bmatrix} \quad (9)$$

$$i_d = i_{od} + i_{cd} \quad (10)$$

$$i_q = i_{oq} + i_{cq} \quad (11)$$

where T is the torque; pp is the number of pole pairs; ψ_f is the rms value of the flux linkage by field; i_{od} and i_{oq} are the magnetizing q -axis and d -axis current, respectively; V_a is the induced voltage; v_d and v_q are the d -axis and q -axis voltage, respectively; R_a is the phase resistance of the armature winding; i_d and i_q are the d -axis and q -axis current, respectively; v_{od} and v_{oq} are the d -axis and q -axis induced voltage; i_{cd} and i_{cq} are the d -axis and q -axis core loss current, respectively. The torque and power according to the rotation speed of the initial model calculated using (6)–(8) are shown in Fig. 11. As shown in Fig. 11, the maximum torque satisfies the target torque within the current limit. However, there is a problem that the torque and power are not satisfied in the high-speed operating region (after 9 kr/min). This is because the induced voltage by the inductance accounts for a large proportion, as shown in the vector diagram of Fig. 12(a). Due to this, the vector of the induced voltage is in the third quadrant in the vector diagram. On the other hand,

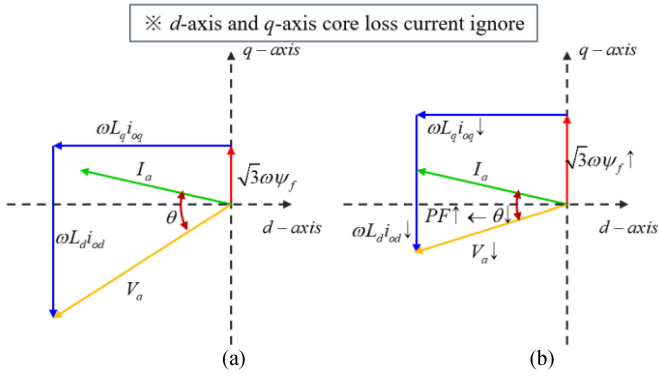


Fig. 12. Vector diagram. (a) Initial model. (b) Design plan of the improved design.

due to the control characteristics of the IPMSM, the vector of the input current is in the second quadrant. Therefore, the phase difference θ between the induced voltage and input current increases, and this phase difference and power factor have the following relationship:

$$\text{PF} = \cos \theta \quad (12)$$

where PF is the power factor. As a result, the power factor in the high-speed operating region is low and the target torque and power in the high-speed operating region are not satisfied. In the following section, the improved design is conducted to expand the satisfactory area of the target torque and power and reduce the DR.

III. IMPROVED DESIGN OF HSML IPMSM

The improved design consists of two steps. The first improved design is to reduce the DR and increase the power factor of the initial model and the second improved design is to reduce the harmonic of the induced voltage of the model designed in the first step.

A. First Improved Design: Reduction of DR and Increase of Power Factor

To expand the satisfactory area of the target power, the power factor should be increased. To increase the power factor, the vector of the induced voltage should be placed in the second quadrant. The design plan to move the vector of the induced voltage to the second quadrant is shown in Fig. 12(b). As shown in Fig. 12(b), the design plan is such that the induced voltage due to the *d*-axis inductance decreases and the induced voltage due to the PM increases. In addition, to reduce the magnitude of the induced voltage, the induced voltage due to the *q*-axis inductance is reduced.

To reduce the DR, this article proposes two methods. The first method is an increase in the thickness of the PM because increasing the thickness of the PM is a common method to prevent the irreversible demagnetization. The second method involves installing a flux barrier between the PM and rib of the rotor. Fig. 13 shows the result of the demagnetization analysis of the initial model. As shown in the white circle of Fig. 13, in

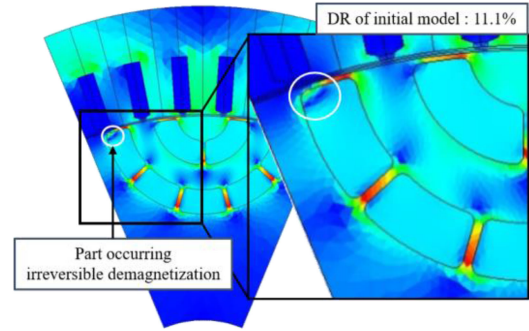
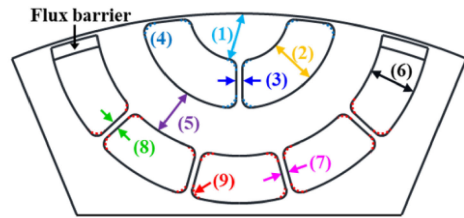


Fig. 13. Result of demagnetization analysis of the initial model.



No.	Variable	Level		
		Low	Middle	High
(1)	1st layer core thickness	3.5	4	4.5
(2)	1st layer PM thickness	8	8.5	9
(3)	1st layer bridge thickness	0.6	0.7	0.8
(4)	1st layer PM fillet radius	1.0	1.25	1.5
(5)	2nd layer core thickness	3.5	4	4.5
(6)	2nd layer PM thickness	8	8.5	9
(7)	2nd layer center bridge thickness	0.8	0.9	1.0
(8)	2nd layer side bridge thickness	0.8	0.9	1.0
(9)	2nd layer PM fillet radius	1.0	1.25	1.5

Fig. 14. Design variables for the ANOVA.

the PMs of the second layer, the irreversible demagnetization of the PM adjacent to the rib of the rotor is particularly severe. This irreversible demagnetization generated in the white circle of Fig. 13 is due to the flux flowing in the rib. Therefore, by placing the flux barrier between the rib and PM, the irreversible demagnetization due to the flux flowing in the rib is prevented. The installed flux barrier can be seen in Fig. 14.

To solve these two problems, the response surface methodology (RSM) is performed on several design variables of the rotor. Before performing the RSM, the design variables that contribute significantly to the design plan are determined using the analysis of variance (ANOVA). The design variables for the ANOVA are shown in Fig. 14. When determining the design variables using the ANOVA, the considerations are the SF, torque at base speed, *d*- and *q*-axis inductance, linkage flux by field, and DR. Fig. 15(a)–(f) shows the contribution ratios of the design variables to the SF, torque, *d*- and *q*-axis inductance, linkage flux by field, and DR, respectively. The design variables, which have a significant effect on the design plan, are selected as the things that have the first and second largest contribution ratios

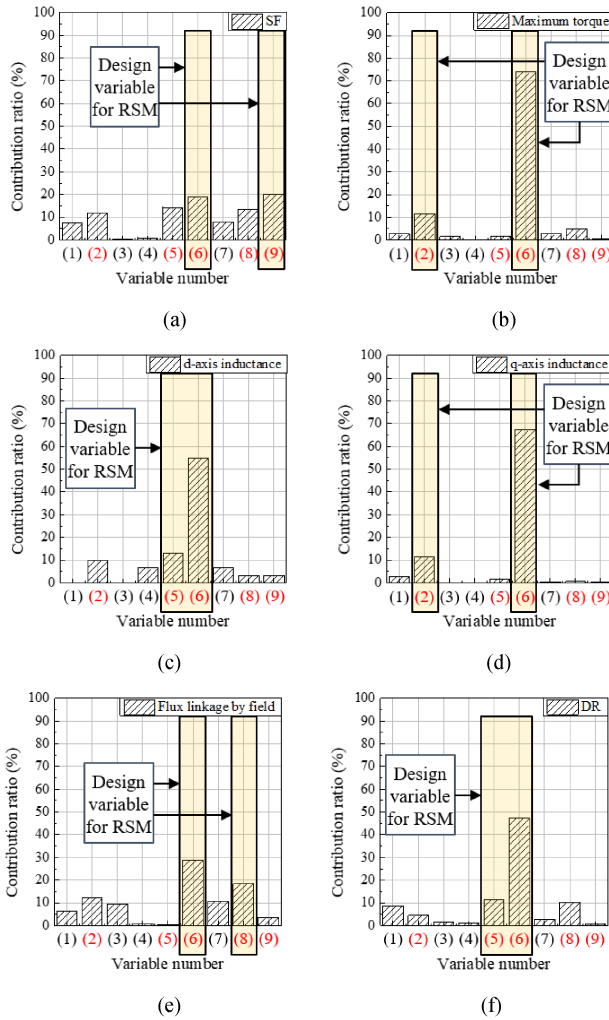


Fig. 15. Contribution ratio according to design variables. (a) SF. (b) Maximum torque. (c) d -axis inductance. (d) q -axis inductance. (e) Flux linkage by field. (f) DR.

for each design plan. As shown in Fig. 15(a)–(f), the selected design variables are as follows.

- 1) (2) is the thickness of the first layer PM.
- 2) (5) is the thickness of the second layer core.
- 3) (6) is the thickness of the second layer PM.
- 4) (8) is the thickness of the second layer side bridge.
- 5) (9) is the fillet radius of the second layer PM.

The values of the other design variables are determined based on the trend of the main effects plot of six considerations of each design variable and they are selected to be 4, 0.6, 1.5, and 0.9 mm, in the order of variable number. The RSM is performed using the selected design variables through the ANOVA. The objective functions and design constraints are shown in Fig. 16. Since an increase in the power factor causes a decrease in the reluctance torque, the efficiency decreases in the constant torque region. Therefore, to prevent a significant reduction in motor efficiency in the constant torque region, maximizing the torque at the base speed was selected as one of the objective functions of the first improved design. The result of the RSM is given in Table III. As given in Table III, the SF and DR of the first improved model are

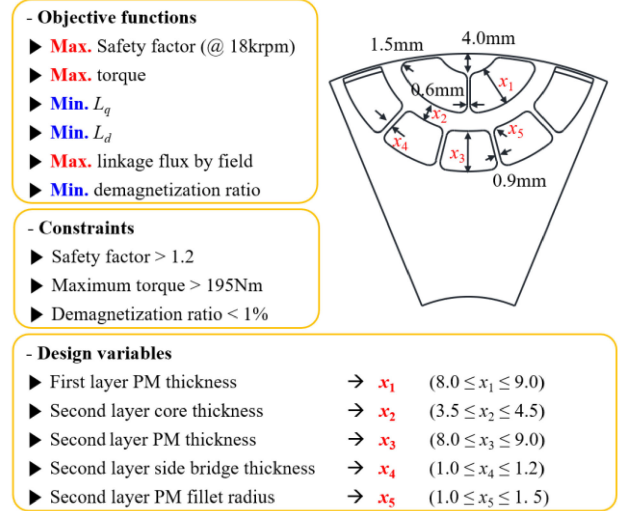


Fig. 16. Objective function, design constraints, and design variables of RSM.

TABLE III
RESULT OF FIRST IMPROVED DESIGN

Content	Unit	Initial	1st Improved
1st layer PM thickness	mm	6.0	8.5
2nd layer core thickness	mm	6.0	3.5
2nd layer PM thickness	mm	6.0	8.6
2nd layer side bridge thickness	mm	0.8	1.0
Fillet radius of 2nd layer PM	mm	1.0	1.5
Normalized PM volume	-	1.0	1.4
Safety factor	-	1.22	1.27
Demagnetization ratio	%	11.1	0.07
Satisfactory area of power	-	0 - 9krpm	All areas

1.27 and 0.07%, respectively. The DR of the improved model is lower than that of the initial model and satisfies the criterion proposed in this article. Fig. 17(a) shows the comparison of the rotor shape between the initial and first improved model, and Fig. 17(b) shows the performance curves of the initial and first improved model. As shown in Fig. 17(b), the torque and power of the first improved model are satisfactory in all areas unlike those of the initial model. This is because of the decrease in the d - and q -axis inductance and the increase in the linkage flux by field, as shown in Fig. 18. Therefore, it can be seen that the improved design is performed in accordance with the desired design plan.

B. Second Improved Design: Reduction of Harmonics in Induced Voltage

Since the current phase angle increases with the increase in the rotation speed, the local magnetic saturation of the motor is also increased. Due to the increase in this local magnetic saturation of the motor, the harmonics of the induced voltage are increased. The desired current cannot be applied to the motor because the increased harmonics of the induced voltage can instantaneously exceed the dc voltage of the controller. Therefore, it is important

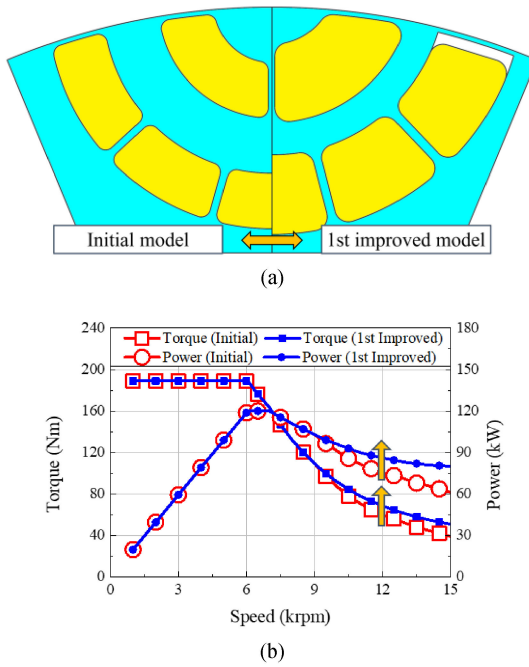


Fig. 17. Comparison of rotor shape and performance curve between the initial and first improved model. (a) Rotor shape. (b) Performance curve.

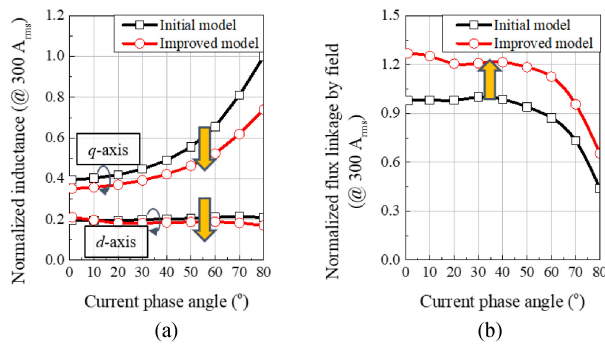


Fig. 18. Parameter comparison between the initial and first improved model. (a) Inductance. (b) Flux linkage by field.

that the induced voltage at the maximum rotation speed does not exceed the dc voltage of the controller. Fig. 19(a) shows the waveform of the induced voltage at the maximum rotation speed. As shown in Fig. 19(a), the peak value of the induced voltage at the maximum rotation speed is approximately 1596 V, whose value exceeds the dc voltage of the controller. Therefore, the second improved design is conducted that the induced voltage does not exceed the dc voltage of the controller. The result of the harmonic analysis of the induced voltage at the maximum rotation speed is shown in Fig. 19(b). As shown in Fig. 19(b), the 11th and 13th components of the induced voltage are significantly larger than other harmonics. To reduce the magnitude of the harmonics of the induced voltage, four methods are applied, that is, changing the number of slots, changing pole angle, the three-step skew of the rotor, and the eccentric rotor shape. The advantages and disadvantages of the four methods are summarized in Fig. 20. First, the number of slots is changed

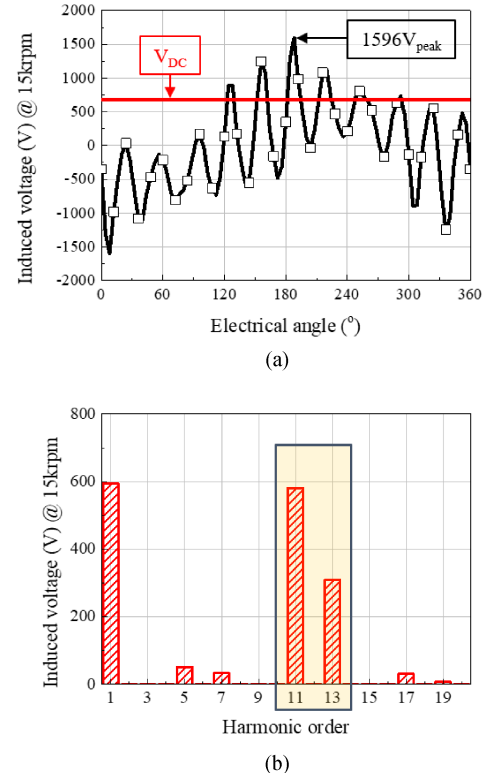


Fig. 19. Induced voltage at the maximum rotation speed of first improved model. (a) Waveform. (b) Harmonic analysis.

Method	Advantage	Disadvantage
The number of slots (N_s)	Pole-angle (PA)	Skew
$N_s \uparrow \rightarrow$ Input voltage ↓	$PA \downarrow \rightarrow$ Induced voltage ↓, SF ↑, Max. torque ↑	Induced voltage ↓, Almost no change in torque
$N_s \uparrow \rightarrow$ Max. torque ↓	$PA \downarrow \rightarrow$ $L_d \& L_q \uparrow, \psi_f \downarrow$	Eccentric length ↑ → Induced voltage ↓, SF ↑
		Higher induced voltage than expected value due to saturation
		Eccentric length ↑ → Max. torque ↓

Fig. 20. Four methods to reduce the induced voltage.

from 48 to 96 to reduce the 11th and 13th component of the induced voltage. This is because the winding factors of the 11th and 13th harmonics of the 8 poles 48 slots are 0.966, while the winding factors of the 11th and 13th harmonics of the 8 poles 96 slots are 0.126. Second, the pole angle is changed from 28° to 27°. Third, the three-step skew is applied to the rotor. At this time, the step skew angle is 2.5° in the mechanical angle to reduce the 11th and 13th component of the induced voltage. Finally, the eccentric rotor shape is applied and the applied eccentric length is 5 mm [1]. The result of the second improved design is summarized in Table IV. The model applying the four methods is called the second improved model. Fig. 21 shows the comparison of the configuration between the first and second improved model, and Fig. 22 shows the induced voltage at the maximum rotation speed of the second improved model. As shown in Fig. 22, the peak value of the induced voltage at the maximum rotation speed of the second improved model is

TABLE IV
RESULT OF SECOND IMPROVED DESIGN

Content	1st improved model	2nd improved model
The number of slots	48	96
Pole-angle	28°	27°
Skew	Not applied	3-step skew (2.5° per step)
Eccentric rotor shape	Not applied	5mm

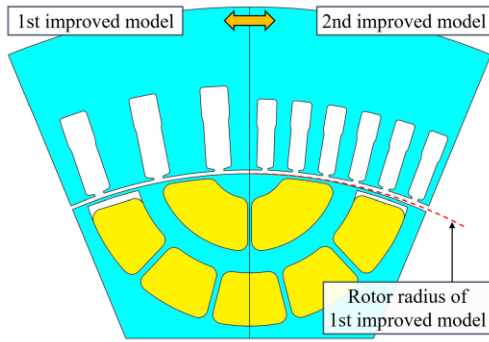


Fig. 21. Comparison of configuration and induced voltage between the first and second improved model.

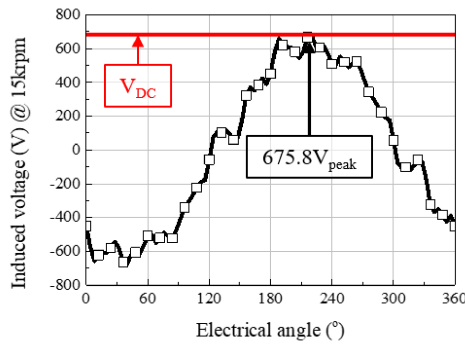


Fig. 22. Induced voltage of the second improved model.

approximately 676 V and does not exceed the dc voltage of the controller. The second improved model is modified to be easy to fabricate the PM, which is described in the following section.

IV. FINAL MODEL OF HSML IPMSM

As mentioned earlier, the second improved model is modified by changing the PM shape. Fig. 23(a) and (b) shows the shapes of the rotors of the second improved model and the final model, respectively. To be easy to fabricate, the first-layer PM shape of the second improved model is modified, as shown in Fig. 23(b). Also, to fix the PMs, a new structure called a guide is additionally made. The SF and DR of the final model are 1.22 and 0.01%, respectively. Fig. 24 shows the mechanical stress distribution and the performance curve of the final model obtained using (6)–(8). As shown in Fig. 24(b), the torque and power of the final model meet the target torque and power in all areas. Also, since the flux weakening control is performed in the high-speed

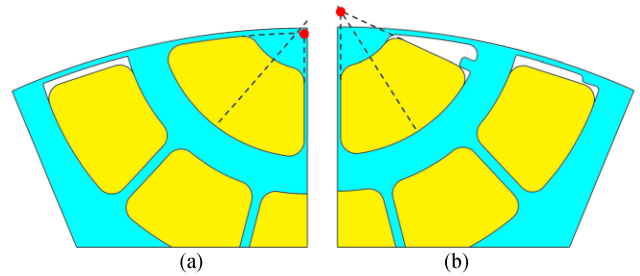


Fig. 23. Rotor shape of the second improved model and final model. (a) Second improved model. (b) Final model.

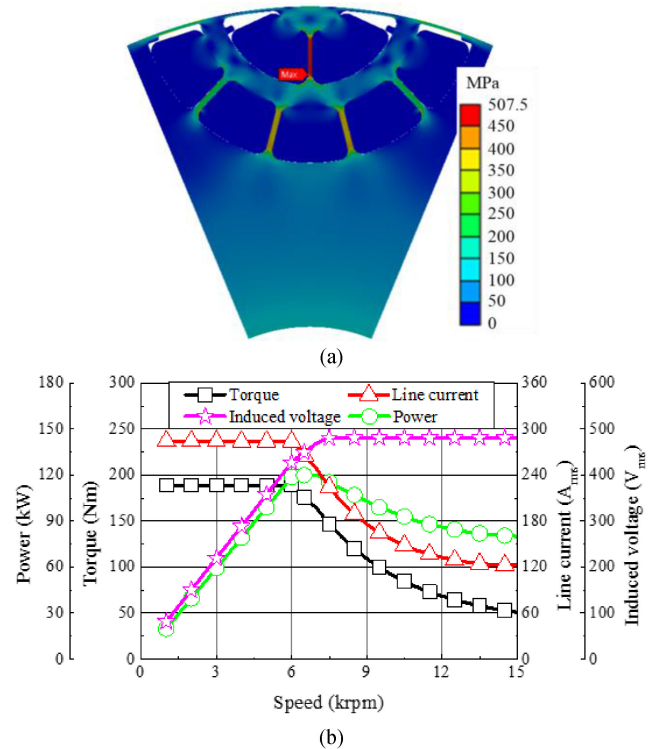


Fig. 24. Mechanical and electrical characteristics of the final model. (a) Mechanical stress distribution. (b) Performance curve.

region by the current vector control, the induced voltage does not exceed the dc voltage and is maintained after 7 kr/min. The information of the final model is summarized in Table V. In Table V, the split ratio and shape ratio are the ratio of the stack length to the outer diameter of the stator and the ratio of the stack length to the outer diameter of the rotor, respectively. The split ratio and shape ratio are expressed as (13) and (14), respectively

$$\text{Split ratio} = \frac{L_{\text{stk}}}{D_s} \quad (13)$$

$$\text{Shape ratio} = \frac{L_{\text{stk}}}{D_r} \quad (14)$$

where L_{stk} is the stack length; D_s is the outer diameter of the stator; D_r is the outer diameter of the rotor.

TABLE V
INFORMATION OF FINAL MODEL

Content	Unit	Value
The number of poles	-	8
The number of slots	-	96
Split ratio	-	0.54
Shape ratio	-	0.74
Safety factor	-	1.22
Demagnetization ratio	%	0.01
Satisfactory area of power	-	All areas

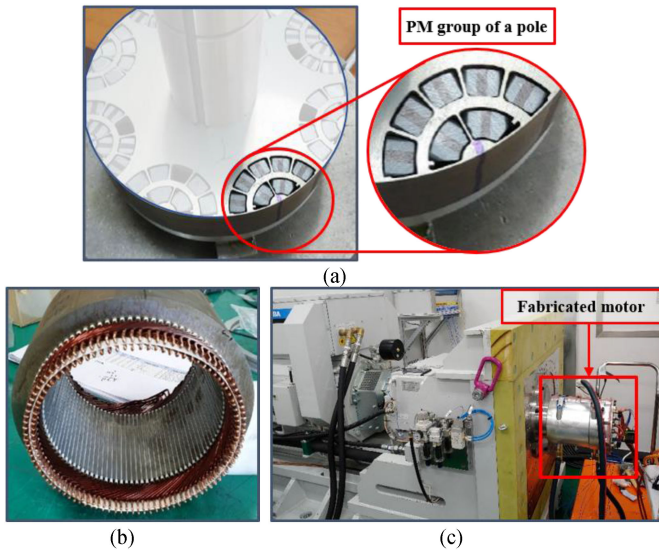


Fig. 25. Fabricated motor and experimental setup. (a) Rotor. (b) Stator. (c) Experimental setup.

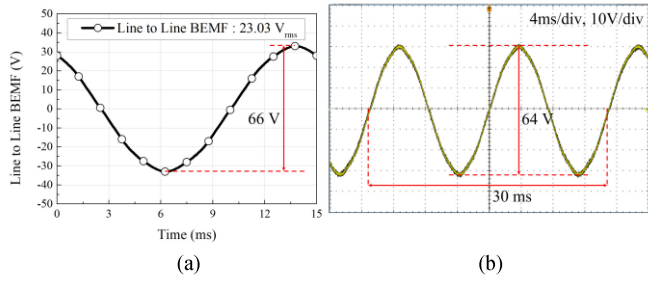


Fig. 26. No-load line to line BEMF. (a) FEA. (b) Experiment.

V. VERIFICATION

To validate the result of the design, the final model is manufactured and experimented. Fig. 25(a) and (b) shows the fabricated rotor and stator, respectively. The PM group of a pole can be seen in Fig. 25(a) and the PM group of a pole is arranged in eight poles. The test motor is connected to the load through the torque sensor and coupling. The performance of the final model is measured using a power analyzer and the measured experimental results are compared with those of the FEA. Fig. 25(c) shows the experimental setup. The no-load experiment is measured at 1000 r/min. Fig. 26 shows the FEA and experimental results

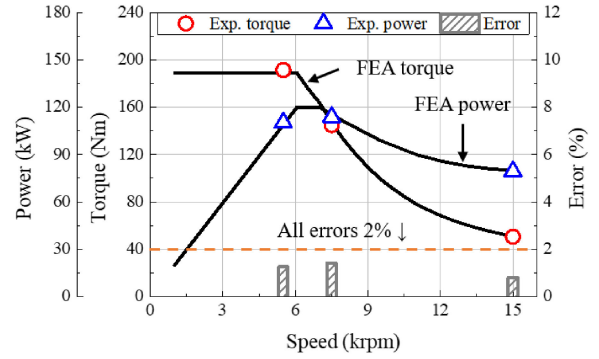


Fig. 27. Torque and power comparison of experiment and FEA.

TABLE VI
RESULT OF LOAD EXPERIMENT AND FEA

Speed (rpm)	Load condition (A _{rms} / °)	Category	Torque (Nm)	Power (kW)	Eff. (%)
5500	283.9 / 48.7	FEA	189.0	108.9	89.5
		Exp.	191.4	110.2	90.2
7500	224.4 / 47.7	FEA	146.9	115.4	92.6
		Exp.	144.9	113.8	92.8
15000	122.2 / 66.4	FEA	50.9	80.0	90.0
		Exp.	50.5	79.4	92.6

of the no-load line-to-line BEMF of the final model. As shown in Fig. 26, the FEA and experimental results of the line-to-line BEMF are 23.03 V_{rms} and 22.63 V_{rms}, respectively, and the error between the FEA and test results is 1.77%. The load experiment is conducted at 5.5, 7.5, and 15 kr/min. Fig. 27 shows the torque and power results of the experiment and FEA. The input current conditions of the load experiment are the same as those calculated from the FEA and are summarized in Table VI. As shown in Fig. 27, it can be seen that the torque and power of the experiment are similar to that of the FEA. Compared with the FEA, the result of the experiment at 5.5 kr/min is increased by 1.2%. At 7.5 kr/min and 15 kr/min, the torque and power of the experiment are decreased by 1.4% and 0.8% compared with that of the FEA, respectively. The differences between all the experiments and FEA results are less than 2%. Additionally, the efficiency of the experiments is similar to that of the FEA. The efficiency of the experiment and FEA are indicated in Table VI. Finally, since the fabricated motor was stably driven at a maximum speed of 15 kr/min, the mechanical stability at 15 kr/min is also experimentally verified. From these experimental results, it can be seen that the design of the HSML IPMSM using the ferrite PM applying the proposed design method is well designed to satisfy the target specifications. Therefore, it can be concluded that the proposed design method in this article is an appropriate design method of the HSML IPMSM using the ferrite PM.

VI. CONCLUSION

This article proposed the design method of HSML IPMSM using the ferrite PM. The electrical and mechanical characteristics were considered simultaneously at all design steps.

Especially, the irreversible demagnetization of the ferrite PM and mechanical stability of the rotor were continuously considered during the design. In the initial design, the design variables, such as the pole shape, PM thickness, core thickness, number of PM layers, number of bridges, and bridge thickness were determined considering the DR, torque, and SF. The initial model was improved to reduce the DR, extend the satisfactory area of the power, and satisfy the SF. The first improved model had the problem that the peak value of the induced voltage exceeds the dc voltage of the controller due to the harmonics of the induced voltage. To solve this problem, various methods were applied to the rotor and stator. The final model was then determined considering the assembly and manufacture. The final model was fabricated for verification. The test was conducted under specific speed conditions. The difference between the torque of the experiment and FEA was less than 2%, and the efficiency of the experiment was similar to that of the FEA. The mechanical stability was also confirmed by the experiment at the maximum rotation speed. Therefore, it is concluded that the proposed design method of the HSML IPMSM using ferrite PM is valid.

REFERENCES

- [1] Y.-H. Jung, M.-S. Lim, M.-H. Yoon, J.-S. Jeong, and J.-P. Hong, "Torque ripple reduction of IPMSM applying asymmetric rotor shape under certain load condition," *IEEE Trans. Energy Convers.*, vol. 33, no. 1, pp. 333–340, Mar. 2018.
- [2] M. J. Akhtar and R. J. Behera, "Optimal design of stator and rotor slot of induction motor for electric vehicle applications," *IET Elect. Syst. Transp.*, vol. 9, no. 1, pp. 35–43, Mar. 2019.
- [3] M. O. Gulbahce and D. A. Kocabas, "High-speed solid rotor induction motor design with improved efficiency and decreased harmonic effect," *IET Elect. Power Appl.*, vol. 12, no. 8, pp. 1126–1133, Sep. 2018.
- [4] I. J. Smith and J. Salmon, "High-efficiency operation of an open-ended winding induction motor using constant power factor control," *IEEE Trans. Power Electron.*, vol. 33, no. 12, pp. 10663–10672, Dec. 2018.
- [5] J.-J. Lee, J. Lee, and K.-S. Kim, "Design of a WFSM for an electric vehicle based on a nonlinear magnetic equivalent circuit," *IEEE Trans. Appl. Supercond.*, vol. 28, no. 3, Apr. 2018, Art. no. 5206304.
- [6] M.-S. Lim and J.-P. Hong, "Design of high efficiency wound field synchronous machine with winding connection change method," *IEEE Trans. Energy Convers.*, vol. 33, no. 4, pp. 1978–1987, Dec. 2018.
- [7] W. Liu and T. A. Lipo, "Saliency enhancement of salient pole wound field synchronous machines for variable speed applications," in *Proc. IEEE Int. Electr. Mach. Drives Conf.*, Miami, FL, USA, 2017, pp. 1–7.
- [8] W. Chai, W. Zhao, and B.-I. Kwon, "Optimal design of wound field synchronous reluctance machines to improve torque by increasing the saliency ratio," *IEEE Trans. Magn.*, vol. 53, no. 11, Nov. 2017, Art. no. 8206604.
- [9] S.-W. Hwang, J.-H. Sim, J.-P. Hong, and J.-Y. Lee, "Torque improvement of wound field synchronous motor for electric vehicle by PM-assist," *IEEE Trans. Ind. Appl.*, vol. 54, no. 4, pp. 3252–3259, Jul./Aug. 2018.
- [10] H.-C. Liu *et al.*, "Optimal design of an ultra-premium-efficiency PMA-synchronous reluctance motor with the winding method and stator parameters to reduce flux leakage and minimize torque pulsations," *IEEE Trans. Magn.*, vol. 54, no. 11, Nov. 2018, Art. no. 8207505.
- [11] D.-K. Ngo, M.-F. Hsieh, and T. A. Huynh, "Torque enhancement for a novel flux intensifying PMa-SynRM using surface-inset permanent magnet," *IEEE Trans. Magn.*, vol. 55, no. 7, Jul. 2019, Art. no. 8106108.
- [12] W. Zhao, H. Shen, T. A. Lipo, and X. Wang, "A new hybrid permanent magnet synchronous reluctance machine with axially sandwiched magnets for performance improvement," *IEEE Trans. Energy Convers.*, vol. 33, no. 4, pp. 2018–2029, Dec. 2018.
- [13] E. Carraro, M. Morandin, and N. Bianchi, "Traction PMASR motor optimization according to a given driving cycle," *IEEE Trans. Ind. Appl.*, vol. 52, no. 1, pp. 209–216, Jan./Feb. 2016.
- [14] M.-R. Park, J.-W. Jung, D.-Y. Kim, J.-P. Hong, and M.-S. Lim, "Design of high torque density multi-core concentrated flux-type synchronous motors considering vibration characteristics," *IEEE Trans. Ind. Appl.*, vol. 55, no. 2, pp. 1351–1359, Mar./Apr. 2019.
- [15] J.-H. Park *et al.*, "Design and verification for the torque improvement of a concentrated flux-type synchronous motor for automotive applications," *IEEE Trans. Ind. Appl.*, vol. 55, no. 4, pp. 3534–3543, Jul./Aug. 2019.
- [16] A. Fatemi, D. M. Ionel, M. Popescu, Y. C. Chong, and N. A. O. Demerdash, "Design optimization of a high torque density spoke-type PM motor for a formula E race drive cycle," *IEEE Trans. Ind. Appl.*, vol. 54, no. 5, pp. 4343–4354, Sep./Oct. 2018.
- [17] L. Xu, W. Zhao, G. Liu, and C. Song, "Design optimization of a spoke-type permanent-magnet vernier machine for torque density and power factor improvement," *IEEE Trans. Veh. Technol.*, vol. 68, no. 4, pp. 3446–3456, Apr. 2019.
- [18] D.-K. Lim *et al.*, "Analysis and design of a multi-layered and multi-segmented interior permanent magnet motor by using an analytic method," *IEEE Trans. Magn.*, vol. 50, no. 6, Jun. 2014, Art. no. 8201308.
- [19] A. R. Tariq, C. E. Nino-Baron, and E. G. Strangas, "Iron and magnet losses and torque calculation of interior permanent magnet synchronous machines using magnetic equivalent circuit," *IEEE Trans. Magn.*, vol. 46, no. 12, pp. 4073–4080, Dec. 2010.
- [20] L. Zhu, S. Z. Jiang, Z. Q. Zhu, and C. C. Chan, "Analytical modeling of open-circuit air-gap field distributions in multisegment and multilayer interior permanent-magnet machines," *IEEE Trans. Magn.*, vol. 45, no. 8, pp. 3121–3130, Aug. 2009.
- [21] J. K. Tangudu, T. M. Jahns, A. El-Refaie, and Z. Q. Zhu, "Lumped parameter magnetic circuit model for fractional-slot concentrated-winding interior permanent magnet machines," in *Proc. IEEE Energy Convers. Congr. Expo.*, San Jose, CA, USA, 2009, pp. 2423–2430.
- [22] J.-W. Jung, B.-H. Lee, K.-S. Kim, and J.-P. Hong, "Design of IPMSM for reduction of eddy current loss in permanent magnets to prevent irreversible demagnetization," in *Proc. IEEE Int. Electr. Mach. Drives Conf.*, Miami, FL, USA, 2017, pp. 1–6.
- [23] T. Tanaka and I. Miki, "IPMSM with ferrite magnets for high speed," in *Proc. 18th Int. Conf. Elect. Mach. Syst.*, Pattaya, Thailand, 2015, pp. 214–217.
- [24] Y.-H. Jung, K.-O. Kim, and J.-P. Hong, "Design of multi-layer IPMSM using ferrite pm considering mechanical and electrical characteristics," in *Proc. IEEE Energy Convers. Congr. Expo.*, Baltimore, MD, USA, 2019, pp. 3534–3541.
- [25] K.-S. Kim, K.-S. Kim, B.-H. Lee, and B.-H. Lee, "Design of concentrated flux synchronous motor to prevent irreversible demagnetization," in *Proc. IEEE Int. Electr. Mach. Drives Conf.*, Miami, FL, USA, 2017, pp. 1–6.
- [26] M.-R. Park, H.-J. Kim, Y.-Y. Choi, J.-P. Hong, and J.-J. Lee, "Characteristics of IPMSM according to rotor design considering nonlinearity of permanent magnet," *IEEE Trans. Magn.*, vol. 52, no. 3, Mar. 2016, Art. no. 8101904.
- [27] R. G. Budynas, *Advanced Strength and Applied Stress Analysis*, 2nd ed. New York, NY, USA: McGraw-Hill, 1999, pp. 498–596.
- [28] F. R. Ismagilov, N. Uzhevog, V. E. Vavilov, V. I. Bekuzin, and V. V. Ayguzina, "Multidisciplinary design of ultra-high-speed electrical machines," *IEEE Trans. Energy Convers.*, vol. 33, no. 3, pp. 1203–1212, Sep. 2018.
- [29] F. Zhang, G. Du, T. Wang, G. Liu, and W. Cao, "Rotor retaining sleeve design for a 1.12-MW high-speed PM machine," *IEEE Trans. Ind. Appl.*, vol. 51, no. 5, pp. 3675–3685, Sep./Oct. 2015.
- [30] K.-S. Cha, D.-M. Kim, M.-R. Park, M.-H. Yoon, and J.-P. Hong, "Multipolar high-speed IPMSM design for EV traction considering mechanical stress," in *Proc. IEEE 84th Veh. Technol. Conf.*, Montreal, QC, Canada, 2016, pp. 1–6.
- [31] T. A. Lipo, *Introduction to AC Machine Design*, 3rd ed. Hoboken, NJ, USA: Wiley, 2017, pp. 181–189.



Young-Hoon Jung received the bachelor's degree in mechanical engineering, and the integrated master's and Ph.D. degrees in automotive engineering from Hanyang University, Seoul, South Korea, in 2013 and 2020.

His research interests are electric machine design for automotive and robot applications, and ultrahigh speed motors.



Min-Ro Park received the bachelor's degree in electrical engineering from Chungnam National University, Daejeon, South Korea, in 2013, and the integrated master's and Ph.D. degrees in automotive engineering from Hanyang University, Seoul, South Korea, in 2020.

Since 2020, he has been with the Korea Institute of Robotics and Technology Convergence, Pohang, South Korea, where he is currently a Senior Researcher. His research interests include multiphysics analysis and design of the electric machine for mechatronics systems.



Jung-Pyo Hong (Senior Member, IEEE) received the Ph.D. degree in electrical engineering from Hanyang University, Seoul, South Korea, in 1995.

From 1996 to 2006, he was a Professor with Changwon National University, Changwon, South Korea. From 2006 to 2019, he had been a Professor with the Hanyang University, Seoul, South Korea. His research interests include the design of electric machines, and the optimization and numerical analysis of electromechanics.



Ki-O Kim received the bachelor's degree in electrical engineering from Soongsil University, Seoul, South Korea, in 2017. He is currently working toward the Ph.D. degree in automotive engineering from Hanyang University, Seoul, South Korea.

His research interests are the design of electric machines and analysis of the electric machine for the electromechanical system.



Myung-Seop Lim (Member, IEEE) received the bachelor's degree in mechanical engineering and the master's and Ph.D. degrees in automotive engineering from Hanyang University, Seoul, South Korea, in 2012, 2014, and 2017, respectively.

From 2017 to 2018, he was a Research Engineer with Hyundai Mobis, Yongin, South Korea. From 2018 to 2019, he was an Assistant Professor with Yeo-ungnam University, Gyeongsan, South Korea. Since 2019, he has been with Hanyang University, Seoul, South Korea, where he is currently an Assistant

Professor. His research interests include electromagnetic field analysis and multiphysics analysis of electric machinery for mechatronics systems, such as automotive and robot applications.



Jun-Woo Chin received the bachelor's degree in mechanical engineering in 2014 from Hanyang University, Seoul, South Korea, where he is currently working toward the Ph.D. degree in automotive engineering.

His research interests are the design of electric machines, and the loss and thermal analysis of electric motor and generator.